

## HIGH-REDSHIFT BLAZARS THROUGH *NuSTAR* EYES

L. MARCOTULLI<sup>1</sup>, V. S. PALIYA<sup>1</sup>, M. AJELLO<sup>1</sup>, A. KAUR<sup>1</sup>, D. H. HARTMANN<sup>1</sup>, D. GASPARRINI<sup>2,3</sup>, J. GREINER<sup>4</sup>, A. RAU<sup>4</sup>, P. SCHADY<sup>4</sup>, M. BALOKOVIĆ<sup>5</sup>, D. STERN<sup>6</sup>, G. MADEJSKI<sup>7</sup>

<sup>1</sup>Department of Physics and Astronomy, Clemson University, Kinard Lab of Physics, Clemson, SC 29634-0978, USA

<sup>2</sup>Agenzia Spaziale Italiana (ASI) Science Data Center, I-00133 Roma, Italy

<sup>3</sup>Istituto Nazionale di Fisica Nucleare, Sezione di Perugia, I-06123 Perugia, Italy

<sup>4</sup>Max Planck Institute für extraterrestrische Physik, Giessenbachstrasse 1, 85748, Garching, Germany

<sup>5</sup>Cahill Center for Astronomy and Astrophysics, California Institute of Technology, Pasadena, CA 91125, USA

<sup>6</sup>Jet Propulsion Laboratory, California Institute of Technology, Pasadena, CA 91109, USA

and

<sup>7</sup>Kavli Institute for Particle Astrophysics and Cosmology, SLAC National Accelerator Laboratory, Menlo Park, CA 94025, USA

### ABSTRACT

The most powerful sources among the blazar family are MeV blazars. Often detected at  $z > 2$ , they usually display high X- and  $\gamma$ -ray luminosities, larger-than-average jet powers and black hole masses  $\gtrsim 10^9 M_\odot$ . In the present work we perform a multiwavelength study of three high redshift blazars: 3FGL J0325.5+2223 ( $z = 2.06$ ), 3FGL J0449.0+1121 ( $z = 2.15$ ), and 3FGL J0453.2–2808 ( $z = 2.56$ ), analysing quasi simultaneous data from GROND, *Swift*-UVOT and XRT, *NuSTAR*, and *Fermi*-LAT. Our main focus is on the hard X-ray band recently unveiled by *NuSTAR* (3–79 keV) where these objects show a hard spectrum which enables us to constrain the inverse Compton peak and the jet power. We found that all three targets resemble the most powerful blazars, with the synchrotron peak located in the sub-millimeter range and the inverse Compton peak in the MeV range, and therefore belong to the MeV blazar class. Using a simple one zone leptonic emission model to reproduce the spectral energy distributions, we conclude that a simple combination of synchrotron and accretion disk emission reproduces the infrared-optical spectra while the X-ray to  $\gamma$ -ray part is well reproduced by the inverse Compton scattering of low energy photons supplied by the broad line region. The black hole masses for each of the three sources are calculated to be  $\gtrsim 4 \times 10^8 M_\odot$ . The three studied sources have jet power at the level of, or beyond, the accretion luminosity.

*Keywords:* galaxies: active — gamma rays: galaxies — quasars: individual (3FGL J0325.5+2223, 3FGL J0449.0+1121, 3FGL J0453.2-2808) — galaxies: jets

### 1. INTRODUCTION

Blazars are a subset of active galactic nuclei (AGN) whose relativistic jets are pointed towards the observer ( $\theta_V < 1/\Gamma$ ,  $\theta_V$  being the viewing angle and  $\Gamma$  the bulk Lorentz factor). From their optical properties, they have been sub-classified

as flat spectrum radio quasars (FSRQs), if their spectrum shows broad emission lines (equivalent width,  $EW > 5\text{\AA}$ ), and BL Lacertae (BL Lac) objects which show weak ( $EW < 5\text{\AA}$ ) or absent emission lines (Stickel et al. 1991; Stocke et al. 1991). Blazars are known to radiate over the entire electromagnetic spectrum, from the low-energy radio band to very high-energy  $\gamma$ -rays; this radiation is primarily due to non-thermal emission processes and is believed to be the mani-

festation of a powerful relativistic jet (e.g., Blandford & Rees 1978; Urry & Padovani 1995; Dermer & Giebels 2016). The spectral energy distribution (SED) of a blazar displays two characteristic broad humps, one peaking between infrared (IR) and X-ray frequencies and the other between the X-ray and  $\gamma$ -ray energy bands. The low-energy hump is attributed to the synchrotron process of relativistic electrons present in the jet, while the high-energy peak is associated with the inverse Compton (IC) scattering of low-energy photons by relativistic electrons. The low-energy photons can be either synchrotron photons (synchrotron self Compton or SSC; Konigl 1981) or photons originating externally to the jet (external Compton or EC; Begelman & Sikora 1987).

Two features are noteworthy: due to the peculiar orientation of the relativistic jet, the enhancement ascribed to relativistic beaming allows us to detect blazars at high redshifts. Moreover, according to the so-called ‘blazar sequence’ (Fossati et al. 1998; Ghisellini et al. 1998), the efficiency of electron cooling due to IC increases with increasing source luminosity. These arguments imply that the more distant and luminous the object is, the greater the shift of the SED humps towards lower frequencies. The synchrotron peak of the most powerful blazars is located in the sub-millimeter (mm) range, while the IC peak falls in the MeV band. The position of the latter classifies such objects as ‘MeV blazars’ (e.g., Bloemen et al. 1995). The characteristics of their spectra have allowed us to detect blazars up to  $z \geq 5$  (e.g., Romani et al. 2004; Sbarrato et al. 2013).

The shift of the IC peak makes MeV blazars bright at hard X-rays ( $> 10$  keV) (see, e.g., Ghisellini 2013). With the advent of the first focusing hard X-ray telescope in orbit, the *Nuclear Spectroscopic Telescope Array* (*NuSTAR*; Harrison et al. 2013), it is now possible to explore the hard X-ray (3–79 keV) energy band with unprecedented detail. *NuSTAR* has already been shown to be a powerful instrument for the study of the most luminous and distant blazars, opening a window to understand the early X-ray universe (e.g., Sbarrato et al. 2013). Thanks to its sensitivity, it has allowed us to investigate some peculiar X-ray features of high-redshift blazars, like variability (e.g. Sbarrato et al. 2016) or flattening in the spectrum (e.g., Paliya et al. 2016). Also, by combining *NuSTAR* observations with *Fermi*-Large Area Telescope (*Fermi*-LAT; Atwood et al. 2009) data, we can more reliably measure the location of the IC peak in the SED. Since the bolometric luminosity of blazars is dominated by high-energy emission (e.g., Ghisellini et al. 2014), an accurate measurement of the IC component in the SED provides important constraints on the power of the jet and on the relativistic particle population. Moreover, the shift in the synchrotron peak reveals the underlying optical-UV thermal emission from the accretion disk (e.g., Ghisellini et al. 2010). Modeling the disk emission with a standard optically thick, spatially thin geometry (Shakura & Sunyaev 1973), one can estimate the central black hole mass and the ac-

cretion disk luminosity. As a result, MeV blazars are ideal objects to study the accretion-jet connection. Furthermore, these sources generally host extremely massive black holes at their centers ( $M_{\text{BH}} \gtrsim 10^9 M_{\odot}$ , e.g., Ghisellini et al. 2010; Ajello et al. 2016; Paliya et al. 2016). This has important implications as the detection of a blazar implies the existence of  $2\Gamma^2$  such sources (where  $\Gamma \sim 10$ –15, e.g., Sikora et al. 1997) with misaligned jets at the same redshift, hosting similarly massive black holes. Therefore a detailed study of MeV blazars, hosting extremely massive black holes, places useful constraints on the high end of the black-hole mass function, which is essential for a full theoretical understanding of the growth and evolution of black holes over cosmic time (e.g., Johnson & Haardt 2016). This can be accomplished by adopting a multi-wavelength approach and utilizing data from a variety of instruments.

Here we present a broadband study of three high-redshift blazars: 3FGL J0325.5+2223 ( $z = 2.06$ ), 3FGL J0449.0+1121 ( $z = 2.15$ ), and 3FGL J0453.2–2808 ( $z = 2.56$ ). These are among the most powerful known sources of this class: found at  $z > 2$  with a  $\gamma$ -ray luminosity  $L_{\gamma} > 10^{46}$  erg s $^{-1}$  (Ackermann et al. 2015), they are soft  $\gamma$ -ray emitters but display a hard X-ray continuum (2–10 keV) (e.g., Ajello et al. 2009; Ghisellini et al. 2011), which classifies them as MeV blazars. They are among the few of their class that are detected in X-rays and by the *Fermi*-LAT as well.

In fact, they have been selected as they are the only three sources, among the ten most luminous LAT FSRQs (Ackermann et al. 2015), which do not have hard X-ray coverage. Therefore we report their first  $E > 10$  keV detection obtained from *NuSTAR* observations<sup>1</sup>. As such it becomes possible to accurately determine the location of the high-energy peak in their SEDs.

Our primary motivation is to understand their physical properties by means of a multi-frequency data analysis and theoretical SED modeling, with a major focus on the hard X-ray observations. All three sources have been simultaneously observed by *NuSTAR*, *Swift* X-Ray Telescope (XRT; Burrows et al. 2005) and *Swift*-UltraViolet and Optical Telescope (UVOT; Roming et al. 2005). Thus, the X-ray energy band was fully covered from 0.3 up to 79 keV. To cover the infrared (IR) to ultra-violet (UV) part of the SEDs, we integrated the observations from *Swift*-UVOT with the ones from the Gamma-Ray Burst Optical/Near-Infrared Detector (GROND; Greiner et al. 2008); for two of the sources these were carried out within one week of *NuSTAR* observations, while for 3FGL J0453.2–2808 they were taken within six

<sup>1</sup> These three sources were observed by *NuSTAR* as part of our cycle program (proposal number 1285; obs IDs: 60101078002, 60101079002, 60101080002).

months, due to technical issues. We also analyze the recently released Pass 8 data from *Fermi*-LAT, which provides better sensitivity at lower energies (Atwood et al. 2013) compared to previously released datasets. Throughout, we use cosmological parameters  $H_0 = 71 \text{ km s}^{-1} \text{ Mpc}^{-1}$ ,  $\Omega_m = 0.27$ , and  $\Omega_\Lambda = 0.73$  (Komatsu et al. 2009).

## 2. OBSERVATIONS

### 2.1. *Fermi*

The LAT Pass 8 data used in this work covers the period of *NuSTAR* observations. Since all three objects are faint in  $\gamma$ -rays, we chose a large time bin (MJD 57082–57448) to generate a meaningful SED. Moreover, there is no significant  $\gamma$ -ray variability detected from these sources<sup>2</sup>, and therefore, the selected period is a reasonable choice.

We followed the standard data reduction procedure as given in the online documentation<sup>3</sup> with a few modifications. In the energy range 0.06–300 GeV, we only selected SOURCE class events (evclass=128), including all four point spread function (PSF) event types lying within a  $15^\circ$  region of interest (ROI) centered at the target source. We used a relational filter “DATA\_QUAL>0”, && “LAT\_CONFIG==1” to define good time intervals. Only the events with zenith angle of  $70^\circ$ ,  $75^\circ$ ,  $85^\circ$  and  $90^\circ$  (according to the PSF types) were included in the analysis in order to avoid contamination from Earth-limb  $\gamma$ -rays. We performed a component-wise data analysis to account for different PSF types and considered the third catalog of *Fermi*-LAT detected sources (3FGL; Acero et al. 2015) to generate a source model. The source model includes all the sources present within the ROI, a Galactic diffuse emission component (gll\_iem\_v06.fits) and isotropic emission models (iso\_P8R2\_SOURCE\_V6\_PSF#\_v06.txt, where #: 0, 1, 2, and 3) (Acero et al. 2016). A combined fitting was performed using the summed likelihood method included in the pyLikelihood library of the ScienceTools to derive the strength of the  $\gamma$ -ray signal. This was accomplished by computing a maximum likelihood test statistic  $TS = 2\Delta \log(\mathcal{L})$  where  $\mathcal{L}$  represents the likelihood function, between models with and without a point source at the position of the object (Mattox et al. 1996). Since we were using data below 100 MeV, we enabled the energy dispersion corrections for all sources, except for the diffuse backgrounds. We performed a first round of optimization to obtain a best initial guess of the spectral parameters for all sources. We then allowed the spectral parameters of all the sources having  $TS > 25$  and lying within  $10^\circ$  from the center of the ROI to vary during the fitting. In the source spectra, only spectral bins where the source was

detected with  $TS > 9$  are reported.

### 2.2. *NuSTAR*

The blazar 3FGL J0325.5+2223 was observed by *NuSTAR* on 2015 November 8 for a net exposure of 22.2 ks; 3FGL J0449.0+1121 was observed on 2015 December 2 for a net exposure of 20.5 ks; and 3FGL J0453.2–2808 was monitored on 2015 December 3 for a net exposure of 19.5 ks. The data for both *NuSTAR* Focal Plane Modules (FPMA and FPMB; Harrison et al. 2013) were processed using the *NuSTAR* Data Analysis Software (NUSTARDAS) v1.5.1. We calibrated the event data files using the task *nupipeline*, with the response file taken from the latest Calibration Database (CALDB). The generation of source and background spectra, ancillary and response matrix files, has been achieved using the *nuproducts* script. We selected circles with radii of  $30''$  centered on the target sources as the source regions and the background events were extracted from circles with the same area but from a nearby source-free region on the same frame.

### 2.3. *Swift*

*Swift*-XRT (Burrows et al. 2005) and UVOT (Roming et al. 2005) observations were carried out simultaneously with *NuSTAR* monitoring. 3FGL J0325.5+2223 was observed on 2015 November 8, whereas 3FGL J0449.0+1121 and 3FGL J0453.2–2808 were monitored on 2015 December 2 and December 3, respectively. The exposure time for each of the three targets was  $\sim 2$  ks. Due to these short exposure times and the intrinsic faintness of the sources in this band, none of the targets were detected by UVOT.

The *Swift*-XRT observations were executed in the photon counting mode. The XRT data were analysed with the XRT-DAS software package (v.3.0.0) distributed by HEASARC within the HEASoft package (v.6.17). We used the task *xrtpipeline* to calibrate and clean the event files. Using the tool XSELECT, we extracted the source and background regions using circles and annuli centered on the source, respectively. The radii for the two regions were chosen taking into account the difference in count rates for the three objects. For 3FGL J0325.5+2223 we used a circular region of  $45''$  radius, and an annular region of inner radius  $90''$  and outer radius  $190''$ ; for 3FGL J0449.0+1121 we used a circular region of  $12''$  radius, and an annular region of inner radius  $40''$  and outer radius  $140''$ ; and for 3FGL J0453.2–2808 we used a circular region of  $25''$  radius, and an annular region of inner radius  $50''$  and outer radius  $150''$ . The ancillary response files were generated using *xrtmkarf* and the source spectra were rebinned to have at least one count per bin.

### 2.4. *GROND*

<sup>2</sup> We searched for significant  $\gamma$ -ray flux variations using the tool ‘*Fermi* All-sky Variability Analysis’ (FAVA; Ackermann et al. 2013), but found none, at least during the period covered in this work.

<sup>3</sup> <http://fermi.gsfc.nasa.gov/ssc/data/analysis/documentation/>

GROND is a multi-channel imager mounted on the 2.2 m MPG<sup>4</sup> telescope at ESO in La Silla, Chile. It simultaneously observes with seven filters ( $g', r', i', z', J, H, K_s$ ), covering the optical to near-infrared wavelength regime (Greiner et al. 2008). The data analysis procedure is described in detail in Krühler et al. (2008). For the optical filters ( $g', r', i', z'$ ), the point spread function (PSF) photometric technique was employed, whereas the aperture extraction method was applied for the near-infrared ( $J, H, K_s$ ) filters, because of the under-sampled PSF in these bands. The optical filters were calibrated with the SDSS Data Release 8 (Aihara et al. 2011) and the near-IR filters were calibrated with 2MASS stars (Skrutskie et al. 2006). We have corrected for Galactic extinction following Schlafly & Finkbeiner (2011). The resulting magnitudes were converted to the AB magnitude system and are provided in Table 1.

### 3. RESULTS

#### 3.1. X-ray Spectral analysis

The joint *Swift*-XRT (0.3-10 keV) and *NuSTAR* (3.0-79 keV) spectra were simultaneously fitted with XSPEC using the C statistic (Cash 1979). For all three sources we included Galactic absorption ( $N_{\text{H}}$ ) with Galactic neutral hydrogen column densities taken from Kalberla et al. (2005).

A power-law model with absorption fixed at the Galactic value was used in all three cases. We included a multiplicative constant factor to cross-calibrate the three instruments; we kept it equal to 1 for FPMB but left it free to vary for FPMA and *Swift*-XRT. For two of the targets, the difference for FPMA is in the range of 6-7 %, while for *Swift*-XRT it is in the 3-20 % range. This is consistent with what has already been found for other sources (e.g., Madsen et al. 2015). In the case of 3FGL J0449.0+1121, due to poor photon statistics, we decided to keep the cross-calibration constant fixed to 1 for both FPMA and FPMB. Within errors, the cross-normalization constant for *Swift*-XRT is compatible with 1. The results of the spectral fits are provided in Table 1 and Figure 1 shows, as an example, the combined spectrum for 3FGL J0325.5+2223.

#### 3.2. SED modeling

To understand the underlying physical mechanisms powering the relativistic jets of these objects, we reproduced the broadband SEDs using a simple one zone leptonic emission model. The details of the adopted procedure can be found in Ghisellini & Tavecchio (2009) and here it is briefly described. The observed radiation was assumed to originate from a spherical emission region covering the entire cross-section of the jet, located at a distance of  $R_{\text{diss}}$  from the central engine, and moving with the bulk Lorentz factor  $\Gamma$ . The

jet semi opening angle was assumed to be 0.1 rad. The relativistic electron population was assumed to follow a broken power law energy distribution of the following type

$$N(\gamma) \propto \frac{(\gamma_{\text{break}})^{-p}}{(\gamma/\gamma_{\text{break}})^p + (\gamma/\gamma_{\text{break}})^q}. \quad (1)$$

where  $\gamma_{\text{break}}$  is the break energy,  $p$  and  $q$  are the slopes of the particle energy distribution before and after  $\gamma_{\text{break}}$ , respectively. In the presence of a tangled but uniform magnetic field  $B$ , electrons radiate via synchrotron and IC mechanisms. For the IC process, the low energy photons considered are synchrotron photons and photons originating outside the jet. We have considered several AGN components as potential reservoirs of external radiation energy density: (a) the accretion disk emission; (b) the X-ray corona lying above and below the accretion disk, having a cut-off power law spectral shape, and reprocessing 30% of the disk luminosity ( $L_{\text{disk}}$ ); (c) the broad line region (BLR); and (d) the dusty torus. Both the BLR and the torus are considered as spherical shells located at distances  $R_{\text{BLR}} = 10^{17} L_{\text{disk},45}^{1/2}$  cm and  $R_{\text{IR}} = 10^{18} L_{\text{disk},45}^{1/2}$  cm, respectively, where  $L_{\text{disk},45}$  is the accretion disk luminosity in units of  $10^{45}$  erg s<sup>-1</sup>. They are assumed to re-emit 10% and 50% of  $L_{\text{disk}}$  and their spectral shapes are considered as a blackbody peaking at the Lyman-alpha frequency and  $T_{\text{IR}}$ , respectively, where  $T_{\text{IR}}$  is the characteristic temperature of the torus. The EC spectra were calculated by deriving the comoving frame radiative energy densities from these components. Finally, we evaluated various powers that the jet carries in the form of the magnetic field ( $P_m$ ), electrons ( $P_e$ ), radiation ( $P_r$ ), and protons ( $P_p$ ). The  $P_p$  or kinetic jet power was estimated by considering protons to be cold and hence contributing only to the inertia of the jet and having an equal number density to that of relativistic electrons (e.g., Celotti & Ghisellini 2008).

The parameters associated with the SED modeling are given in Table 2 and the results are plotted in Figure 2.

#### 3.3. Black hole mass estimation

The most commonly used approach to calculate quasar black hole mass is adopting a single epoch optical spectroscopic measurement, which assumes that the BLR is virialized (e.g., Shen et al. 2011). Another novel method to derive the black hole mass is by reproducing the IR-UV spectra of quasars with a standard Shakura & Sunyaev (1973) accretion disk, provided the big blue bump is visible in this energy band (see, Ghisellini & Tavecchio 2015). This is particularly useful when the optical/IR spectrum of the source is not available. In this technique, the spectral shape of the accretion disk is assumed as a multi-color blackbody with the following flux density profile (Frank et al. 2002)

$$F_\nu = \nu^3 \frac{4\pi h \cos \theta_\nu}{c^2 D^2} \int_{R_{\text{in}}}^{R_{\text{out}}} \frac{R dR}{e^{h\nu/kT(R)} - 1}, \quad (2)$$

<sup>4</sup> <https://www.eso.org/sci/facilities/lasilla/telescopes/national/2p2.html>

where  $D$  is the distance of the observer,  $k$  is the Boltzmann constant,  $c$  is the speed of light, and  $R_{\text{in}}$  and  $R_{\text{out}}$  are the inner and outer disk radii, taken as  $3R_{\text{Sch}}$  and  $500R_{\text{Sch}}$ , respectively.  $R_{\text{Sch}}$  is the Schwarzschild radius. The radial temperature profile can be given as

$$T(R) = \frac{3R_{\text{Sch}}L_{\text{disk}}}{16\pi\eta_a\sigma_{\text{SB}}R^3} \left[ 1 - \left( \frac{3R_{\text{Sch}}}{R} \right)^{1/2} \right]^{1/4}, \quad (3)$$

where  $\sigma_{\text{SB}}$  is the Stefan-Boltzmann constant and  $\eta_a$  is the accretion efficiency, adopted here as 10%. There are only two parameters, the black hole mass and the accretion rate  $\dot{M}_a$ , to determine. The rate of accretion can be computed from the intrinsic accretion disk luminosity  $L_{\text{disk}} = \eta_a \dot{M}_a c^2$ . Since  $L_{\text{disk}}$  can be obtained from observations, provided the peak of the big blue bump is visible in the SED, this leaves only the black hole mass as a free parameter (e.g., Ghisellini & Tavecchio 2015).

The black hole masses of two out of three sources, 3FGL J0325.5+2223 and 3FGL J0449.0+1121, were derived by Shaw et al. (2012) using the optical spectroscopic approach. Using the C IV line, they found masses of  $1.6 \times 10^9 M_{\odot}$  and  $7.9 \times 10^7 M_{\odot}$  for 3FGL J0325.5+2223 and 3FGL J0449.0+1121, respectively. For 3FGL J0453.2–2808, we used C IV line parameters from Fricke et al. (1983) and adopted the empirical relations of Shen et al. (2011) to derive a central black hole mass of  $\sim 7.9 \times 10^8 M_{\odot}$ . Instead following the SED modeling approach, we found black hole masses for 3FGL J0325.5+2223, 3FGL J0449.0+1121 and 3FGL J0453.2–2808 of  $6.3 \times 10^8$ ,  $5.0 \times 10^8$  and  $1.0 \times 10^9 M_{\odot}$ , respectively (all black-hole masses are listed in Table 3). The black hole masses computed from both approaches reasonably match within a factor of 2 for two of the sources<sup>5</sup>, though the SED modeling predicts a higher black hole mass (factor of  $\sim 6$ ) for 3FGL J0449.0+1121.

#### 4. DISCUSSION

High-redshift blazars are bright targets in hard X-rays. This is probably due to the shift of blazar SED towards longer wavelengths as their non-thermal luminosity increases (Fossati et al. 1999). The shifting causes their spectra to become steeper at  $\gamma$ -rays ( $\Gamma_{\gamma} \gtrsim 2.3$ ) and harder at X-rays ( $\Gamma_X \lesssim 1.5$ ). Indeed, all the three MeV blazars studied here display these features (see Table 1). In this regard, observations in both these energy bands are crucial to determine the power of the jet and explore its connection to accretion. In fact, having both *NuSTAR* and *Fermi*-LAT detections for all three sources provides a unique opportunity to locate the IC peak and study the shape of the underly-

ing electron population. The bolometric emission in such powerful blazars is dominated by high energy X-ray and  $\gamma$ -rays radiation conveying that good quality spectral measurements in both bands are desirable. Furthermore, there are a few other interesting properties of high redshift blazars revealed by *NuSTAR* monitoring. This includes a spectral flattening seen in the joint *Swift*-XRT and *NuSTAR* spectrum of various MeV blazars (Paliya et al. 2016) and also a substantial flux variability seen at two different epochs of *NuSTAR* monitoring (e.g., Tagliaferri et al. 2015). The latter becomes more important due to the fact that these sources are weaker at  $\gamma$ -rays and may not have enough signal to detect significant variability in this energy range. As a result, *NuSTAR* has proved to be a fundamental instrument to pursue high-redshift blazar studies.

The joint XRT and *NuSTAR* spectra of the three sources do not show any curvature within the available statistics and is well fitted by a simple absorbed power law model with  $N_{\text{H}}$  fixed to the Galactic value. It is reported in various recent studies that the 0.3–79 keV X-ray spectra of many MeV blazars ( $> 5$ ) show a distinct curvature or a break around  $\sim$ few keV (e.g. Tagliaferri et al. 2015; Paliya et al. 2016). Such a feature reflects the behavior of the emitting electron distribution, intrinsic to the jet, rather than any other external factors (Paliya et al. 2016, and references therein). On the other hand, there are observations of MeV blazars, that do not show any such feature (e.g. Ajello et al. 2016). In fact, the shape of the X-ray spectrum constrains the behavior of the underlying electron population, especially the low energy cut-off of the electrons ( $\gamma_{\text{min}}$ ) provided the X-ray emission is dominated by EC process, rather than by SSC (see, e.g., Celotti & Ghisellini 2008). This is illustrated in Figure 3. As can be seen, a good fit can be achieved only with  $\gamma_{\text{min}} \sim 1$ . For higher values, the model predicts a significant break in the X-ray spectrum, which is not seen<sup>6</sup>. This implies the joint XRT and *NuSTAR* observations are instrumental in evaluating the minimum energy of the underlying particle population, which ultimately controls the jet power.

The broadband SEDs of the three MeV sources resemble those of powerful blazars. The synchrotron peaks lie in the sub-mm range, whereas the high-energy IC peaks lie in the MeV band. The Compton dominance (the ratio of IC to synchrotron peak luminosities) is found to be  $>1$  for all three blazars. The GROND observations reveal a break in the IR-optical spectra of the sources which we interpret as a combination of the falling synchrotron spectrum and the rising

<sup>5</sup> It should be noted that the typical errors in virial spectroscopic black hole mass calculation is  $\sim 0.4$  dex (e.g., Vestergaard & Peterson 2006; Shen et al. 2011)

<sup>6</sup> We caution that our calculations at low values of  $\gamma$  are rather approximate. These relatively ‘cold’ electrons could be involved in bulk Compton process (Celotti et al. 2007) and one should self-consistently take this into account. However, this feature is yet to be observed (however see, Ackermann et al. 2012, for a possible detection) and so its contribution is uncertain. Furthermore, the kinetic jet power is very sensitive to  $\gamma_{\text{min}}$  and for  $\gamma_{\text{min}} \gg 1$  it falls below the jet power in radiation, which is problematic for powerful FSRQs (see, e.g. Ghisellini et al. 2014)

accretion disk radiation. Though we do not see the peak of the disk emission (primarily due to lack of UV data), based on the shape of the GROND spectra and the available archival broad line luminosities (Fricke et al. 1983; Shaw et al. 2012), we are able to derive both the disk luminosity and the central black hole mass. Another constraint is provided by the broader limiting range of the disk luminosity that can be set by considering  $10^{-2}L_{\text{Edd}} < L_{\text{disk}} < L_{\text{Edd}}$ . The upper limit ensures the source to be sub-Eddington and the lower limit assumes the accretion disk is radiatively efficient. Furthermore, combining the observations from *Swift*-XRT, *NuSTAR* and *Fermi*, we can cover the X- and  $\gamma$ -ray portions of the spectrum. These parts of the SEDs are successfully reproduced by IC scattering of low energy photons produced externally to the jet.

Since in the adopted model the radiative energy densities of various AGN components are functions of the distance from the central engine, we are able to determine the location of the emission region. This is found to be at the outer edge of the BLR where a major fraction of the seed photons are supplied by the BLR clouds. The X-ray spectra of all three objects are extremely hard and observations further hint at the dominance of the EC process over SSC emission in this energy range (see, Ajello et al. 2016, for a detailed discussion). On the other hand, the  $\gamma$ -ray SEDs are steep, as expected in high redshift blazars. The spectral shapes observed at X-ray and  $\gamma$ -ray energies help constrain the slopes of the underlying broken power law electron energy distribution. Overall, the observed SED parameters of these three sources are similar to other high-redshift MeV blazars (e.g., Ghisellini et al. 2010).

With good quality IR-optical (constraining the accretion disk emission) and hard X-ray- $\gamma$ -ray data (required for the accurate measurement of the jet power) in hand, it is interesting to compare the disk-jet connection observed in the three MeV blazars studied in this work with that for other blazars. With this in mind, we collect the jet powers and disk luminosities of all blazars studied by Ghisellini et al. (2014). In Figure 4, we plot the jet power as a function of the disk luminosity for blazars, including our three MeV sources. The plotted quantities are normalized for the central black hole mass. As can be seen, the majority of sources have normalized jet power exceeding their normalized disk luminosities (the one-to-one correlation is shown by the green solid line). 3FGL J0325.5+2223 and 3FGL J0453.2–2808 have their jet powers larger than their disk luminosities, though 3FGL J0449.0+1121 lies just below the one-to-one correlation. Indeed, among the three objects, this object has the least jet power. The jet powers of both 3FGL J0325.5+2223 and 3FGL J0453.2–2808 appear to be larger than the Eddington luminosity ( $P_{\text{jet}}/L_{\text{Edd}} > 1$ ). However, there are a few caveats. The existence of electron-positron pairs in the jet would reduce the jet power by  $n_e/n_p$  (where  $n_e \equiv n_{e^-} + n_{e^+}$ , see, Pjanka et al. 2017, for a detailed discussion), although

their number could not greatly exceed the protons in order to avoid the Compton rocket effect that would otherwise stop the jet (Ghisellini & Tavecchio 2010). Furthermore, the budget of the jet power can also come down if one considers a spine-sheath structured jet, instead of a one-zone uniform emission region (Sikora et al. 2016). Most importantly, the underestimation of the black hole mass can also lead to super-Eddington jet power. Consequently, one has to take into account these uncertainties and/or their combination before drawing any firm conclusion.

## 5. CONCLUSIONS

We studied three high redshift ( $z > 2$ ) MeV blazars using quasi-simultaneous GROND, *Swift*, *NuSTAR*, and *Fermi*-LAT data, focusing on the hard X-ray part uncovered by *NuSTAR*. With the latter and the aid of the *Fermi*-LAT data we were able to constrain the position of the IC peak and to derive related characteristics of these sources like bolometric luminosity, jet power as well as the relativistic particle distribution and the location of the emission region. Our primary findings are as follows

1. All sources are significantly detected by *NuSTAR* and exhibit a flat (photon index  $\lesssim 1.5$ ) X-ray spectrum extended up to 79 keV, as revealed from joint XRT and *NuSTAR* fitting.
2. The broadband SEDs of these sources resembles that of powerful blazars with synchrotron and IC peaks lying at sub-mm and MeV energy ranges, respectively.
3. The IR-optical spectra can be explained by a combination of synchrotron and accretion disk spectrum, whereas, high energy X-ray to  $\gamma$ -ray radiation is successfully reproduced by IC scattering of low energy photons mainly supplied by the BLR.
4. The location of the emission region is found to be at the outer edge of the BLR in all three sources. The black hole masses for all three sources are greater than  $10^{8.6} M_{\odot}$ .
5. Comparing the normalized jet powers and disk luminosities of these sources with that of a large sample of blazars, we find them to lie on the well known disk-jet correlation derived by Ghisellini et al. (2014) where their jet powers exceeds accretion disk luminosities. Only 3FGL J0449.0+1121 shows a slight offset from this correlation.

We are thankful to the referee for a constructive report. The *Fermi* LAT Collaboration acknowledges generous ongoing support from a number of agencies and institutes that have supported both the development and the operation of the LAT as well as scientific data analysis. These include the

National Aeronautics and Space Administration and the Department of Energy in the United States, the Commissariat à l’Energie Atomique and the Centre National de la Recherche Scientifique / Institut National de Physique Nucléaire et de Physique des Particules in France, the Agenzia Spaziale Italiana and the Istituto Nazionale di Fisica Nucleare in Italy, the Ministry of Education, Culture, Sports, Science and Technology (MEXT), High Energy Accelerator Research Organization (KEK) and Japan Aerospace Exploration Agency (JAXA) in Japan, and the K. A. Wallenberg Foundation, the Swedish Research Council and the Swedish National Space Board in Sweden. Additional support for science analysis during the operations phase is gratefully acknowledged from the Istituto Nazionale di Astrofisica in Italy and the Centre National d’Études Spatiales in France.

This *NuSTAR* work was supported under NASA Contract No. NNG08FD60C, and made use of data from the *NuSTAR* mission, a project led by the California Institute of Technology, managed by the Jet Propulsion Laboratory, and funded by the National Aeronautics and Space Administration. We thank the *NuSTAR* Operations, Software and Cali-

bration teams for support with the execution and analysis of these observations. This research has made use of the *NuSTAR* Data Analysis Software (NuSTARDAS) jointly developed by the ASI Science Data Center (ASDC, Italy) and the California Institute of Technology (USA).

We thank the *Swift* team and the Swift PI (N. Gehrels) for promptly scheduling and executing the observations.

Part of this work is based on archival data, software or online services provided by the ASI Data Center (ASDC). This research has made use of the XRT Data Analysis Software (XRTDAS). Part of the funding for GROND (both hardware and personnel) was generously granted by the Leibniz-Prize to G. Hasinger (DFG grant HA 1850/28-1).

We acknowledge funding from NASA contract NNX15AV09G. M.B. acknowledges support from NASA Headquarters under the NASA Earth and Space Science Fellowship Program, grant NNX14AQ07H.

Part of the funding for GROND (both hardware as well as personnel) was generously granted from the Leibniz-Prize to Prof. G. Hasinger (DFG grant HA 1850/28-1).

## REFERENCES

- Acerro, F., Ackermann, M., Ajello, M., et al. 2015, *ApJS*, 218, 23
- Acerro, F., Ackermann, M., Ajello, M., et al. 2016, *The Astrophysical Journal Supplement Series*, 223, 26
- Ackermann, M., Ajello, M., Ballet, J., et al. 2012, *ApJ*, 751, 159
- Ackermann, M., Ajello, M., Albert, A., et al. 2013, *ApJ*, 771, 57
- Ackermann, M., Ajello, M., Atwood, W. B., et al. 2015, *ApJ*, 810, 14
- Aihara, H., Allende Prieto, C., An, D., et al. 2011, *ApJS*, 193, 29
- Ajello, M., Costamante, L., Sambruna, R. M., et al. 2009, *ApJ*, 699, 603
- Ajello, M., Ghisellini, G., Paliya, V. S., et al. 2016, *ApJ*, 826, 76
- Atwood, W., Albert, A., Baldini, L., et al. 2013, arXiv:1303.3514, arXiv:1303.3514
- Atwood, W. B., Abdo, A. A., Ackermann, M., et al. 2009, *ApJ*, 697, 1071
- Begelman, M. C., & Sikora, M. 1987, *ApJ*, 322, 650
- Blandford, R. D., & Rees, M. J. 1978, *PhysJ*, 17, 265
- Bloemen, H., Bennett, K., Blom, J. J., et al. 1995, *A&A*, 293
- Burrows, D. N., Hill, J. E., Nousek, J. A., et al. 2005, *SSRv*, 120, 165
- Cash, W. 1979, *ApJ*, 228, 939
- Celotti, A., & Ghisellini, G. 2008, *MNRAS*, 385, 283
- Celotti, A., Ghisellini, G., & Fabian, A. C. 2007, *MNRAS*, 375, 417
- Dermer, C. D., & Giebels, B. 2016, *Comptes Rendus Physique*, 17, 594
- Fossati, G., Celotti, A., Ghisellini, G., & Maraschi, L. 1999, in *Astronomical Society of the Pacific Conference Series*, Vol. 159, BL Lac Phenomenon, ed. L. O. Takalo & A. Sillanpää, 351
- Fossati, G., Maraschi, L., Celotti, A., Comastri, A., & Ghisellini, G. 1998, *MNRAS*, 299, 433
- Frank, J., King, A., & Raine, D. J. 2002, *Accretion Power in Astrophysics*, by Juhan Frank and Andrew King and Derek Raine, pp. 398. ISBN 0521620538. Cambridge, UK: Cambridge University Press, February 2002
- Fricke, K. J., Kollatschny, W., & Witzel, A. 1983, *A&A*, 117, 60
- Ghisellini, G. 2013, *Mem. Soc. Astron. Italiana*, 84, 719
- Ghisellini, G., Celotti, A., Fossati, G., Maraschi, L., & Comastri, A. 1998, *MNRAS*, 301, 451
- Ghisellini, G., & Tavecchio, F. 2009, *MNRAS*, 397, 985
- . 2010, *MNRAS*, 409, L79
- . 2015, *MNRAS*, 448, 1060
- Ghisellini, G., Tavecchio, F., Maraschi, L., Celotti, A., & Sbarrato, T. 2014, *Nature*, 515, 376
- Ghisellini, G., Della Ceca, R., Volonteri, M., et al. 2010, *MNRAS*, 405, 387
- Ghisellini, G., Tagliaferri, G., Foschini, L., et al. 2011, *MNRAS*, 411, 901
- Greiner, J., Bornemann, W., Clemens, C., et al. 2008, *PASP*, 120, 405
- Harrison, F. A., Craig, W. W., Christensen, F. E., et al. 2013, *ApJ*, 770, 103
- Johnson, J. L., & Haardt, F. 2016, *PASA*, 33, e007
- Kalberla, P. M. W., Burton, W. B., Hartmann, D., et al. 2005, *A&A*, 440, 775
- Komatsu, E., Dunkley, J., Nolte, M. R., et al. 2009, *ApJS*, 180, 330
- Konigl, A. 1981, *ApJ*, 243, 700
- Krübler, T., Küpcü Yoldaş, A., Greiner, J., et al. 2008, *ApJ*, 685, 376
- Madsen, K. K., Harrison, F. A., Markwardt, C. B., et al. 2015, *ApJS*, 220, 8
- Mattox, J. R., Bertsch, D. L., Chiang, J., et al. 1996, *ApJ*, 461, 396
- Paliya, V. S., Parker, M. L., Fabian, A. C., & Stalin, C. S. 2016, *ApJ*, 825, 74
- Pjanka, P., Zdziarski, A. A., & Sikora, M. 2017, *Monthly Notices of the Royal Astronomical Society*, 465, 3506
- Romani, R. W., Sowards-Emmerd, D., Greenhill, L., & Michelson, P. 2004, *ApJL*, 610, L9
- Roming, P. W. A., Kennedy, T. E., Mason, K. O., et al. 2005, *SSRv*, 120, 95
- Sbarrato, T., Tagliaferri, G., Ghisellini, G., et al. 2013, *ApJ*, 777, 147
- Sbarrato, T., Ghisellini, G., Tagliaferri, G., et al. 2016, *MNRAS*, 462, 1542
- Schlafly, E. F., & Finkbeiner, D. P. 2011, *ApJ*, 737, 103
- Shakura, N. I., & Sunyaev, R. A. 1973, *A&A*, 24, 337
- Shaw, M. S., Romani, R. W., Cotter, G., et al. 2012, *ApJ*, 748, 49
- Shen, Y., Richards, G. T., Strauss, M. A., et al. 2011, *ApJS*, 194, 45
- Sikora, M., Madejski, G., Moderski, R., & Poutanen, J. 1997, *ApJ*, 484, 108
- Sikora, M., Rutkowski, M., & Begelman, M. C. 2016, *MNRAS*, 457, 1352
- Skrutskie, M. F., Cutri, R. M., Stiening, R., et al. 2006, *AJ*, 131, 1163
- Stickel, M., Padovani, P., Urry, C. M., Fried, J. W., & Kuehr, H. 1991, *ApJ*, 374, 431
- Stoeck, J. T., Morris, S. L., Gioia, I. M., et al. 1991, *ApJS*, 76, 813
- Tagliaferri, G., Ghisellini, G., Perri, M., et al. 2015, *ApJ*, 807, 167
- Urry, C. M., & Padovani, P. 1995, *PASP*, 107, 803
- Vestergaard, M., & Peterson, B. M. 2006, *ApJ*, 641, 689

**Table 1.** Table of Observations and Spectral Parameters

<i>Fermi-LAT</i>								
Name	Time Covered	Flux <sup>a</sup>	Photon Index <sup>b</sup>	Test Statistic <sup>c</sup>				
3FGL J0325.5+2223	2015-03-01–2016-03-01	$5.57 \pm 1.12$	$2.37 \pm 0.09$	76.36				
3FGL J0449.0+1121	2015-03-01–2016-03-01	$11.90 \pm 1.50$	$2.35 \pm 0.06$	229.62				
3FGL J0453.2–2808	2015-03-01–2016-03-01	$8.11 \pm 1.22$	$2.49 \pm 0.08$	195.91				
<i>NuSTAR + Swift-XRT</i>								
Name	Date	$N_{\text{H}}^d$	Photon Index <sup>e</sup>	Flux <sup>f</sup>	C-Stat/dof			
3FGL J0325.5+2223	2015-11-08	8.92	$1.36^{+0.10}_{-0.09}$	$7.44^{+0.81}_{-1.13}$	643.74/823			
3FGL J0449.0+1121	2015-12-02	12.6	$1.46^{+0.44}_{-0.43}$	$1.05^{+0.40}_{-0.91}$	291.47/331			
3FGL J0453.2–2808	2015-12-03	2.05	$1.52 \pm 0.10$	$6.64^{+0.91}_{-0.70}$	625.66/769			
GROND								
Name	UT Date <sup>g</sup>	AB Magnitude <sup>h</sup>						
		$g'$	$r'$	$i'$	$z'$	$J$	$H$	$K_s$
3FGL J0325.5+2223	2015-11-15.49	$18.91 \pm 0.05$	$18.78 \pm 0.04$	$18.58 \pm 0.05$	$18.25 \pm 0.05$	$18.36 \pm 0.11$	$18.40 \pm 0.13$	$17.91 \pm 0.16$
3FGL J0449.0+1121	2015-12-08.31	$21.17 \pm 0.05$	$18.49 \pm 0.05$	$18.49 \pm 0.04$	$18.32 \pm 0.05$	$17.94 \pm 0.12$	$17.50 \pm 0.14$	$17.05 \pm 0.14$
3FGL J0453.2–2808	2016-06-01.63	$17.35 \pm 0.29$	$17.42 \pm 0.30$	$17.49 \pm 0.29$	$17.37 \pm 0.28$	$16.96 \pm 0.10$	$16.72 \pm 0.12$	$16.49 \pm 0.13$

**Notes:**

<sup>a</sup> Integrated  $\gamma$ -ray flux in the 0.06 – 300 GeV energy range in units of  $10^{-8}$  photons  $\text{cm}^{-2} \text{s}^{-1}$ .

<sup>b</sup> Photon index calculated from  $\gamma$ -ray analysis.

<sup>c</sup> Test statistic is a measure of significance of detection ( $\sigma \sim \sqrt{\text{TS}}$ ; [Mattox et al. 1996](#)).

<sup>d</sup> Column density in units of  $10^{20} \text{ cm}^{-2}$ .

<sup>e</sup> Photon index calculated from X-ray analysis.

<sup>f</sup> Observed flux in units of  $10^{-12} \text{ erg cm}^{-2} \text{ s}^{-1}$  in the 0.3 – 79 keV energy band. The errors are at the 90% level of confidence for one parameter of interest and the fluxes are corrected for the Galactic absorption.

<sup>g</sup> Exposure start time.

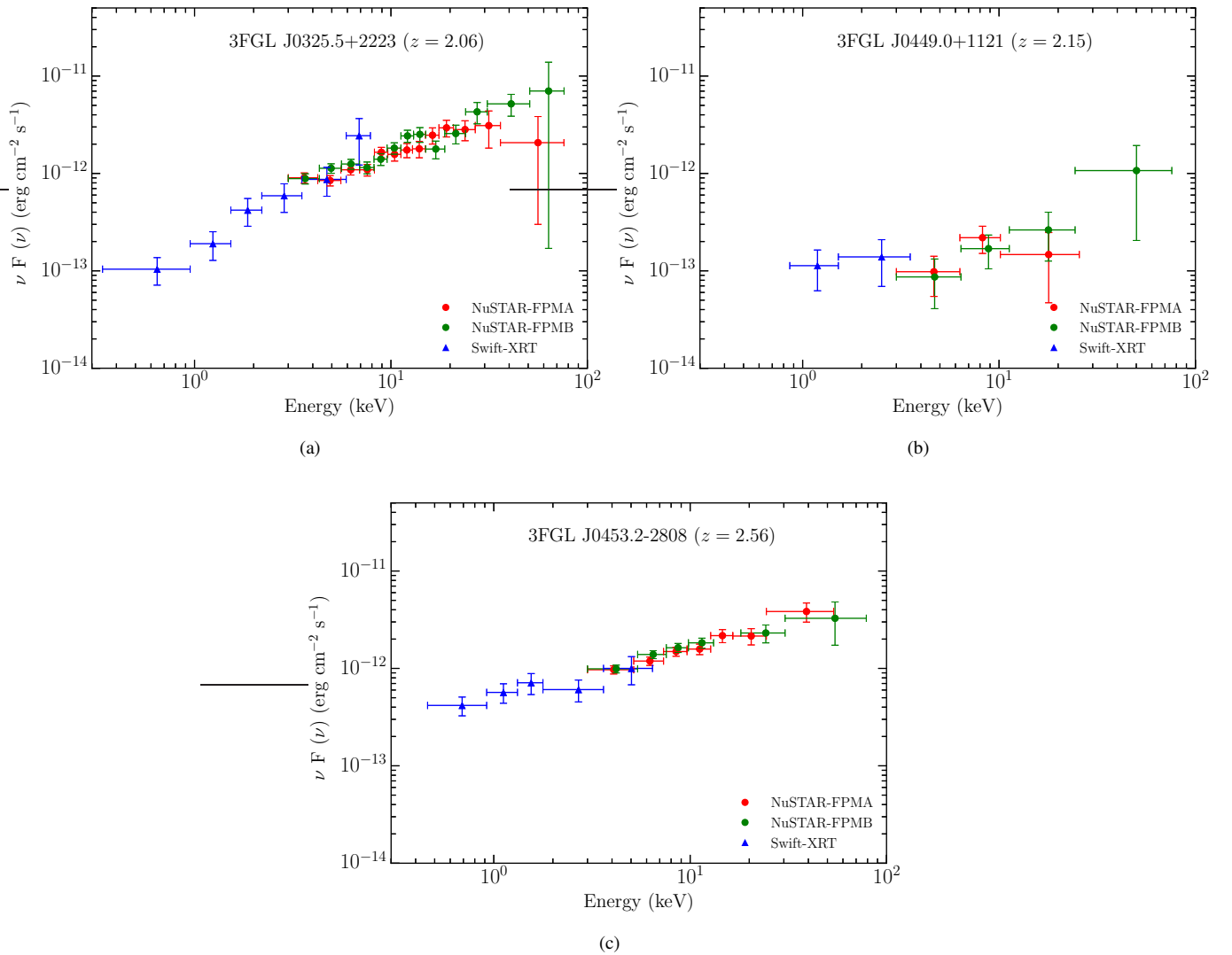
<sup>h</sup> Corrected for Galactic reddening.

**Table 2.** Summary of the parameters used/derived from the SED modeling of three MeV blazars shown in Figure 2. A viewing angle of  $3^\circ$  is adopted for all of them.

Parameter	J0325.5+2223	J0449.0+1121	J0453.2–2808
Slope of the particle distribution below the break energy ( $p$ )	1.45	1.55	1.95
Slope of the particle distribution above the break energy ( $q$ )	3.9	4.15	4.1
Magnetic field in Gauss ( $B$ )	3.2	1.5	2.5
Particle energy density in $\text{erg cm}^{-3}$ ( $U_e$ )	0.03	0.01	0.01
Bulk Lorentz factor ( $\Gamma$ )	10	12	10
Minimum Lorentz factor ( $\gamma_{\text{min}}$ )	1	6	1
Break Lorentz factor ( $\gamma_{\text{break}}$ )	57	310	139
Maximum Lorentz factor ( $\gamma_{\text{max}}$ )	3e3	3e3	3e3
Dissipation distance in parsec ( $R_{\text{Sch}}$ )	0.18 (3090)	0.23 (4850)	0.37 (3900)
Size of the BLR in parsec (in $R_{\text{Sch}}$ )	0.18 (3091)	0.19 (4006)	0.35 (3709)
Black hole mass in log scale, in units of solar mass ( $M_{\text{BH,m}}$ )	8.8	8.7	9.0
Accretion disk luminosity in log scale ( $L_{\text{disk}}$ , $\text{erg s}^{-1}$ )	46.48	46.54	47.08
Accretion disk luminosity in Eddington units ( $L_{\text{disk}}/L_{\text{Edd}}$ )	0.40	0.56	0.95
Characteristic temperature of IR-torus in Kelvin ( $T_{\text{IR}}$ )	500	500	500
Observed variability time scale in days ( $t_{\text{var}}$ )	4	5	10
Jet power in electrons in log scale ( $P_e$ , $\text{erg s}^{-1}$ )	44.87	44.52	44.90
Jet power in magnetic field in log scale ( $P_B$ , $\text{erg s}^{-1}$ )	46.06	45.79	46.49
Radiative jet power in log scale ( $P_r$ , $\text{erg s}^{-1}$ )	45.74	45.60	45.92
Jet power in protons in log scale ( $P_p$ , $\text{erg s}^{-1}$ )	47.18	46.15	47.43

**Table 3.** Table of Black-Hole Masses, derived both from spectroscopic approach and SED modelling.

	3FGL J0325.5+2223	3FGL J0449.0+1121	3FGL J0453.2-2808
$M_{\text{BH,SED}} (M_{\odot})$	$6.3 \times 10^8$	$5.0 \times 10^8$	$1.0 \times 10^9$
$M_{\text{BH,spectroscopy}} (M_{\odot})$	$1.6 \times 10^9$	$7.9 \times 10^7$	$7.9 \times 10^8$

**Figure 1.** Combined *Swift*-XRT and *NuSTAR* (FPMA and FPMB) observations of 3FGLJ0325.5+2223 on 2015 November 11, 3FGLJ04490+1121 on 2015 December 2, and 3FGLJ04532-2808 on 2015 December 3.

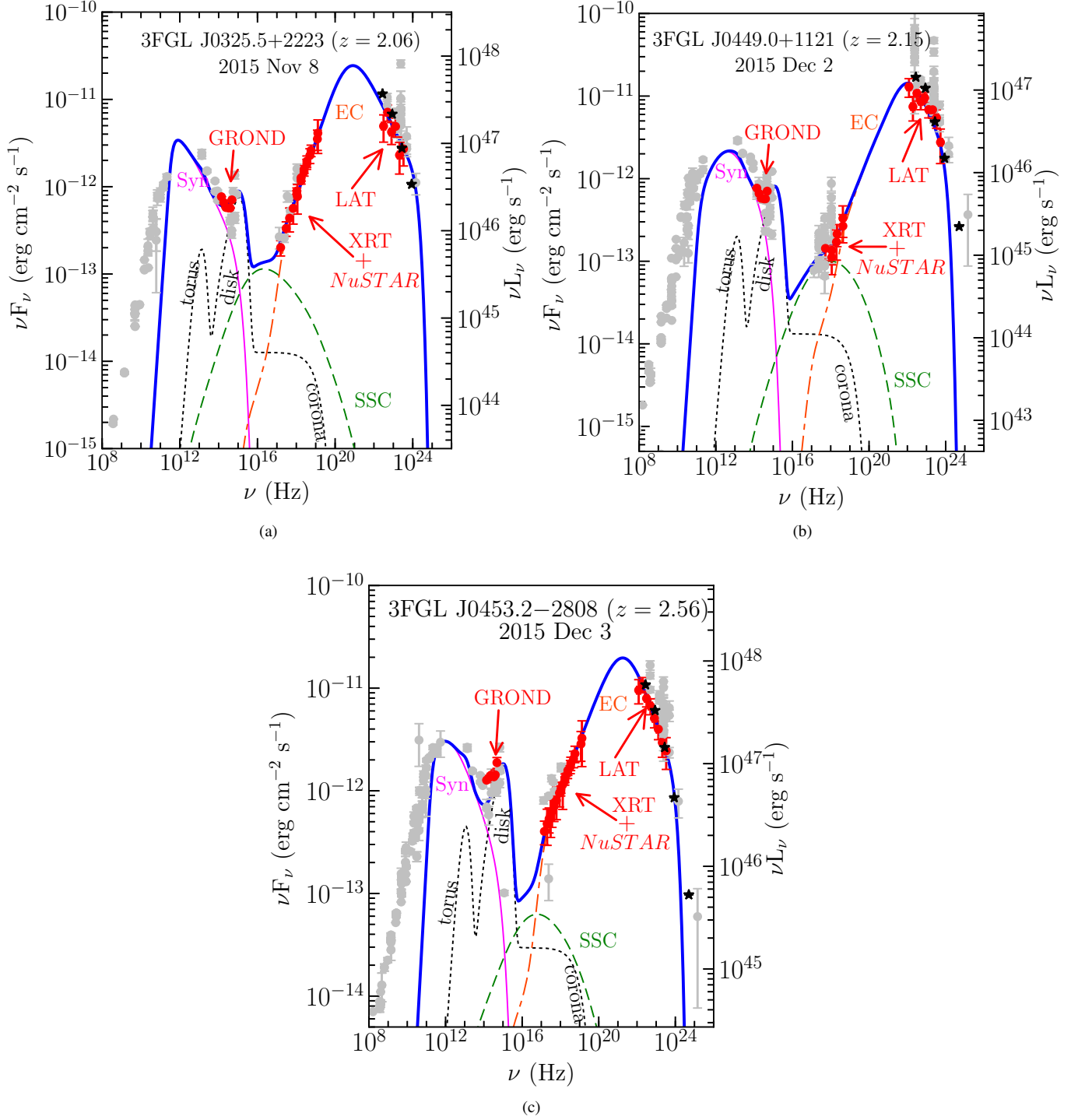


**Figure 2.** The broadband SED of three quasars using quasi-simultaneous GROND, *Swift*, *NuSTAR*, and *Fermi*-LAT data, modeled using the one zone leptonic emission model described in the text. Grey and red circles represent the archival and quasi-simultaneous observations, respectively. In the *Fermi*-LAT energy range, black stars denote the 3FGL spectrum.

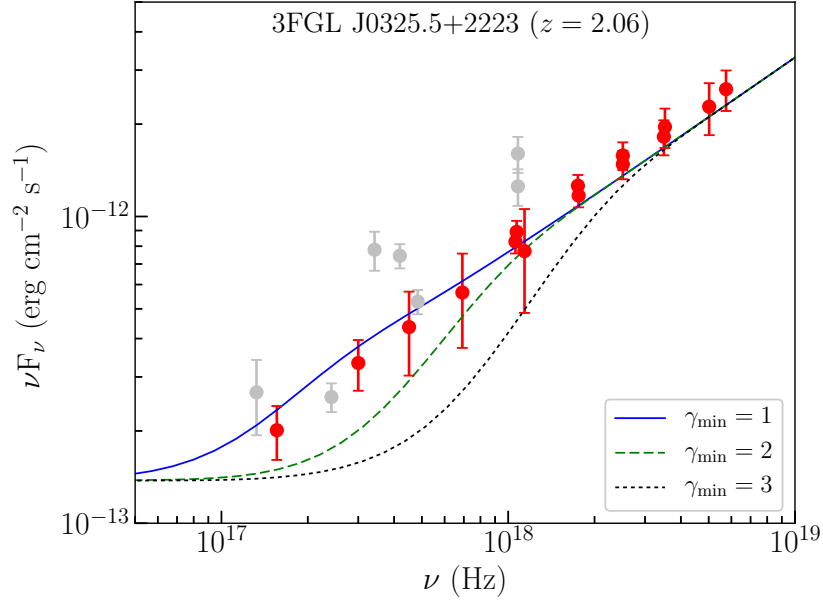


**Figure 3.** Zoomed SED of 3FGL J0325.5+2223, showing the X-ray spectrum. The different lines represent the modeling done with various  $\gamma_{\min}$  values (as labelled). As can be seen, in this source the low-energy cut-off cannot be significantly larger than unity.

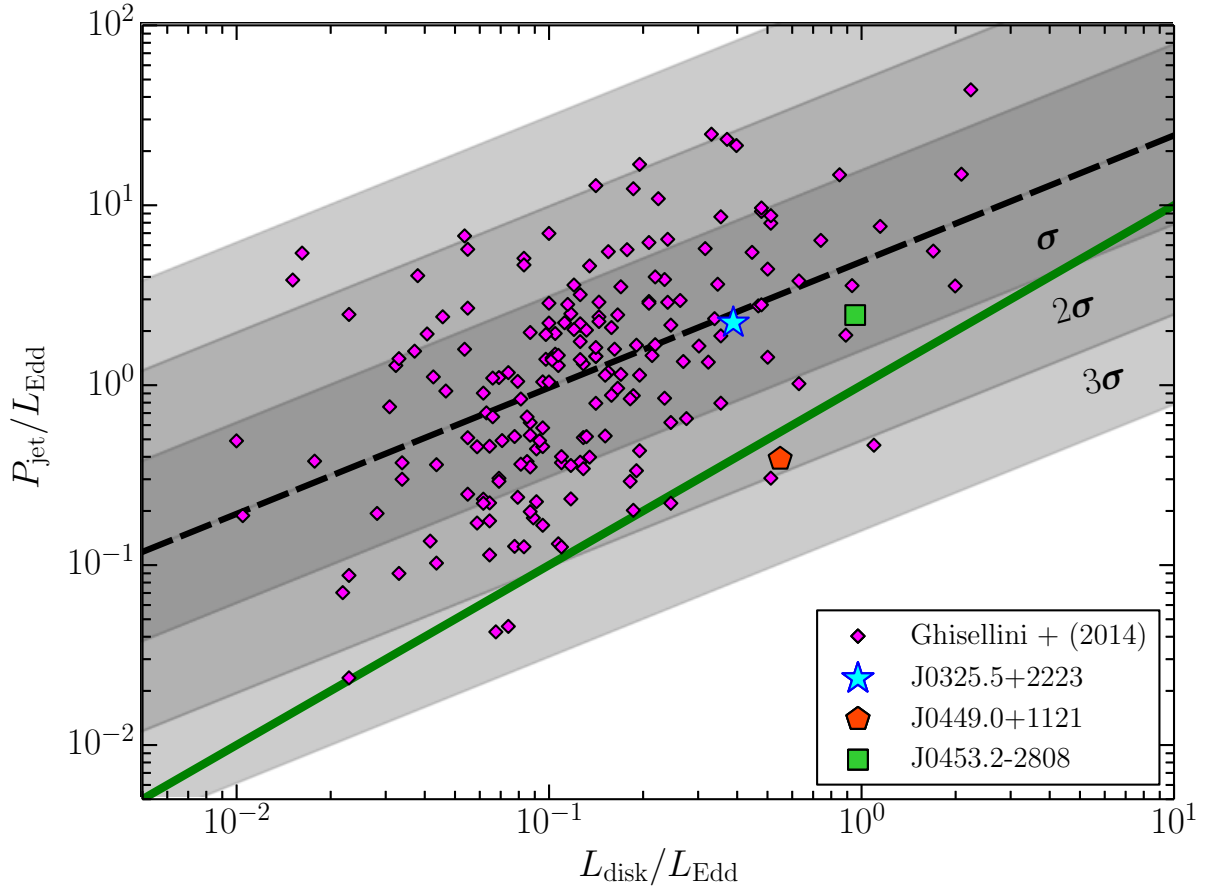


**Figure 4.** Comparison of jet powers and accretion disk luminosities of three MeV sources with that of a large sample of blazars studied by Ghisellini et al. (2014). Black dashed and green solid lines represent the best fit and one-to-one correlation of the plotted quantities, respectively. Both jet powers and disk luminosities are normalized for central black hole mass.